energies

MDPI

Article

CO_2-Free Hydrogen Production by Methane Pyrolysis Utilizing a Portion of the Produced Hydrogen for Combustion

Takuma Uehara, Makoto Asahara * and Takeshi Miyasaka

Department of Mechanical Engineering, Gifu University, 1-1 Yanagido, Gifu 501-1193, Japan; uehara.takuma.p4@s.gifu-u.ac.jp (T.U.); miyasaka.takeshi.m1@f.gifu-u.ac.jp (T.M.)
* Correspondence: asahara.makoto.n8@f.gifu-u.ac.jp; Tel.: +81-58-293-2525

Abstract: Air pollutants such as carbon dioxide and nitrogen oxides emitted by the combustion of fossil fuels have become the subject of increasing concern. Hydrogen has accordingly emerged as a promising low-emission alternative energy source. Among the various methods for hydrogen production, methane pyrolysis, which produces hydrogen without emitting carbon dioxide, has gained substantial attention. This study evaluated the self-sustainability of a new hydrogen production system based on methane pyrolysis, in which a portion of the hydrogen produced is used as combustion fuel rather than relying on catalysts and electrical heating. Coupled heat transfer and one-dimensional reaction simulations employing two plug-flow reactors of a counterflow double-pipe heat exchanger were conducted to investigate the feasibility and efficiency of the proposed system, as well as the influence of flow conditions on hydrogen production. The results confirmed system viability, informed the estimation of hydrogen production rates, and provided methane conversion rate data emphasizing the critical role of low-flow conditions and residence time in system efficiency. Additionally, the production of carbon constituted a significant aspect of system efficiency. These findings indicate that the proposed system can produce environmentally friendly hydrogen, contributing to its potential utilization as a sustainable energy source.

Keywords: hydrogen; methane pyrolysis; hydrogen–air; non-catalytic reaction; double-pipe heat exchanger

Citation: Uehara, T.; Asahara, M.; Miyasaka, T. CO_2-Free Hydrogen Production by Methane Pyrolysis Utilizing a Portion of the Produced Hydrogen for Combustion. *Energies* **2024**, *17*, 367. https://doi.org/10.3390/en17020367

Academic Editor: Eugenio Meloni

Received: 12 December 2023
Revised: 8 January 2024
Accepted: 9 January 2024
Published: 11 January 2024

1. Introduction

Fossil fuels, such as coal, oil, and liquified natural gas, constitute 85% of the world's primary energy sources and, since 2020, provide 61.3% of the world's electricity generation. This figure demonstrates that the world is heavily dependent on fossil fuel combustion [1]. The combustion of fossil fuels emits large quantities of air pollutants, including carbon dioxide and nitrogen oxides. These emissions have become problematic owing to their significant negative impacts on the natural environment and human health [1–4]. This has led to considerable research efforts to eliminate the emission of air pollutants. In particular, hydrogen, which creates only steam as a byproduct when combusted, has attracted attention as a new energy source with a lower environmental and public health impact than fossil fuels, resulting in the development of many hydrogen-related technologies [5,6].

Hydrogen is currently used in large quantities as chemical feedstock for ammonia production, hydrogen refining, hydrogen-reduced steelmaking, and rocket fuel. As hydrogen-related technologies continue to develop, the use of hydrogen will expand to a wider variety of applications, including heating, power generation, fuel cells, and combustion fuel, which will require mass production. Hydrogen production methods, such as steam reforming, biomass gasification, water electrolysis, and pyrolysis, are classified by color based on environmental impact. For example, hydrogen produced by steam reforming is classified as blue hydrogen when the emitted carbon dioxide is captured and stored and as gray hydrogen when the carbon dioxide is not captured [7]. Hydrogen produced by

water electrolysis is classified as green hydrogen, and hydrogen produced by pyrolysis is classified as turquoise hydrogen. Notably, turquoise hydrogen produced by the thermal decomposition (pyrolysis) of methane (the primary component of natural gas) effectively excludes other substances. Consequently, solid carbon is produced instead of gaseous carbon dioxide. This production method is also environmentally friendly because it can employ existing infrastructure and technology to transport raw materials and obtain hydrogen from inexpensive fossil resources without emitting carbon dioxide.

Turquoise hydrogen is produced by reacting methane under high-temperature conditions as follows:

$$CH_4 = 2H_2 + C(\text{solid}) \quad \Delta H^{\circ}_{25^{\circ}C} = +75 \text{ kJ/mol}. \tag{1}$$

Equation (1) indicates that the C-H bond in methane is characterized by a strong covalent bond, implying that the thermal decomposition reaction of methane demands high energy for the cleavage of this bond [8]. As a result, many studies have been conducted using metal catalysts to produce turquoise hydrogen [9–24]. Catalysts supported on high-surface-area ceramic substrates are generally considered effective owing to factors such as increased active sites due to the increased surface area and heat and corrosion resistance due to the ceramic material [16]. However, the significant economic cost of the associated conditioning process has motivated research on the use of unsupported solid metal catalysts [15–28]. Additionally, all catalyst-based methods face issues such as catalyst deactivation [17,25–29] and high costs that can significantly impact the viability of the hydrogen market.

Hydrogen production through the thermal decomposition of methane based on non-catalytic gas-phase reactions requires a high activation energy, as indicated in Equation (1). Therefore, a high reaction temperature is necessary to obtain the energy. However, electric heating is usually used to produce turquoise hydrogen [30–34], and previous studies have indicated that the cost of electricity significantly increases the price of the hydrogen generated (102 USD/kg), making it economically infeasible [35] (generally, assuming no value of carbon, the cost of selling hydrogen in methane pyrolysis is 3.7 USD/kg, compared to 2.2 USD/kg in steam methane reforming [36]). Cheon et al. [37] conducted simulations of a hydrogen production system utilizing a combustion heater and found that, depending on the selling price of carbon, the system was less costly than other turquoise hydrogen production methods involving electric heating, catalysts, and steam methane reforming (blue hydrogen). This implies that combustion-heated methane pyrolysis holds promise for future hydrogen production.

Therefore, in this study, we proposed and evaluated a system that utilizes the combustion of a portion of the produced hydrogen, rather than electricity, as the heat source for pyrolysis. This study employed a numerical model of a double-pipe heat exchanger based on the plug-flow reactor to conduct a series of hydrogen combustion-heated methane pyrolysis simulations that identified the optimal conditions, thus maximizing the feasibility of hydrogen production.

2. Numerical Simulation Methods

In this study, we established a simulation environment for a double-pipe heat exchanger used in combustion-heated methane pyrolysis. In this section, we introduce the numerical calculation method. Detailed chemical reaction calculations were performed using a plug-flow reactor embedded in the Cantera software (ver. 2.6.0). The fluid flowing through the pipes was modeled, and the methane conversion rate (α) and the amount of hydrogen used in combustion (β) (Figure 1) were calculated from the methane flow rate at the inlet and outlet of the outer pipe. During the modeling process, the pipes were divided into finite cells, each treated as a zero-dimensional ideal gas reactor. Furthermore, coupling was incorporated into the model to simulate heat transfer between the inner and outer pipes of the heat exchanger. Section 2.1 introduces the proposed system and simulation model, Section 2.2 discusses the fundamental equations of the plug-flow reactor model,

Section 2.3 presents the basic equations for heat transfer, and Section 2.4 introduces the coupling method for chemical reaction calculations and heat transfer.

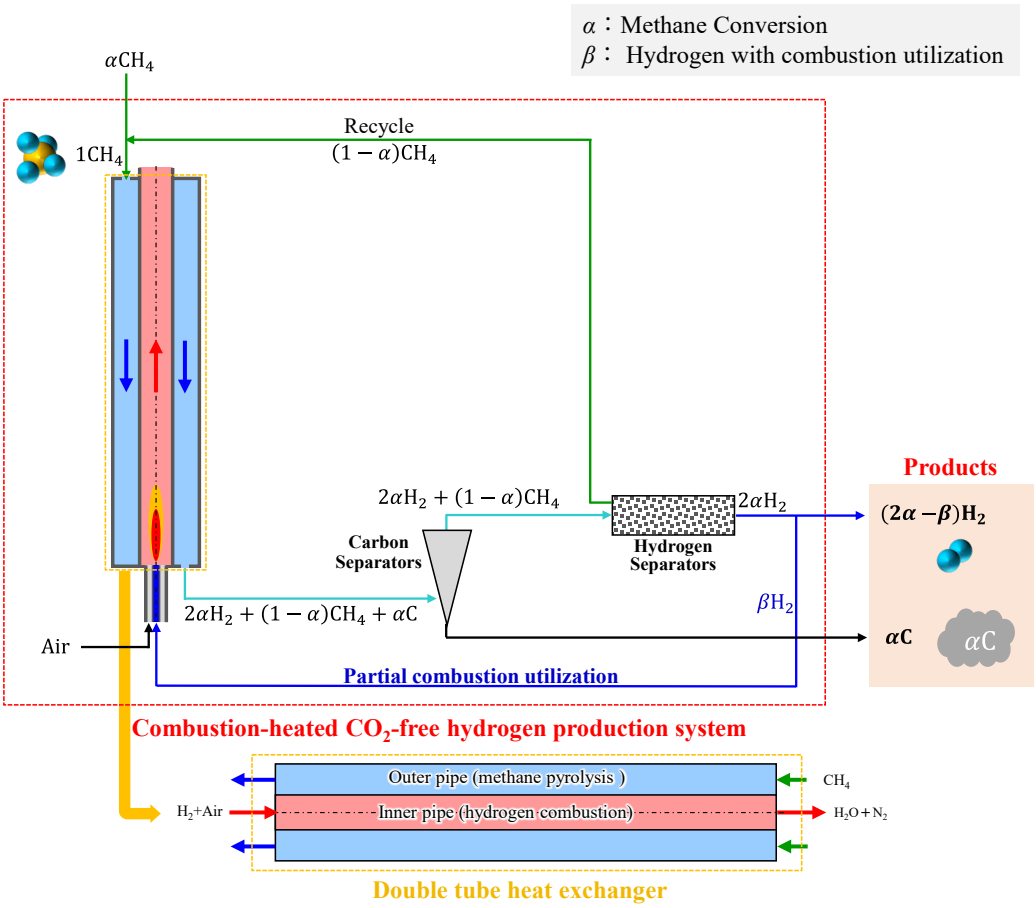

Figure 1. Configuration of combustion-heated methane pyrolysis hydrogen production system.

2.1. Proposed System and Simulation Model

Figure 1 shows a schematic of the proposed hydrogen production system evaluated in this study. The yellow-framed area in the figure indicates where the reaction calculations were undertaken considering a counterflow double-pipe heat exchanger. Since the focus of this study is on the self-sustainability of the system, this study did not consider separation costs and assumed room temperatures for the methane recovered by the system and the combustion spent hydrogen.

The computational model of the counterflow double-pipe heat exchanger is depicted in the lower section of Figure 1. In this study, the inner pipe was supplied with hydrogen fuel and an oxidizer (air) at an equivalence ratio of $\varphi = 1.0$ considering the hydrogen combustion reaction; the outer pipe was supplied with methane (CH_4) as the low-temperature fluid considering the thermal decomposition reactions of methane.

Figure 2 shows a schematic of the counterflow double-pipe heat exchanger employed in this study, where T_{1in} and T_{1out} are the inlet and outlet temperatures on the high-temperature side, respectively, T_{2in} and T_{2out} are the inlet and outlet temperatures on the low-temperature side, respectively, $C_{p,1}$ and $C_{p,2}$ are the specific heat on the high- and low-temperature sides, respectively, Q_{12} is the heat transferred from the outer pipe to the inner pipe, and Q_{23} is the heat loss from the outer pipe to its surroundings. The dimensions of the modeled methane pyrolysis reactor are user parameters described in the calculation conditions in Section 3.

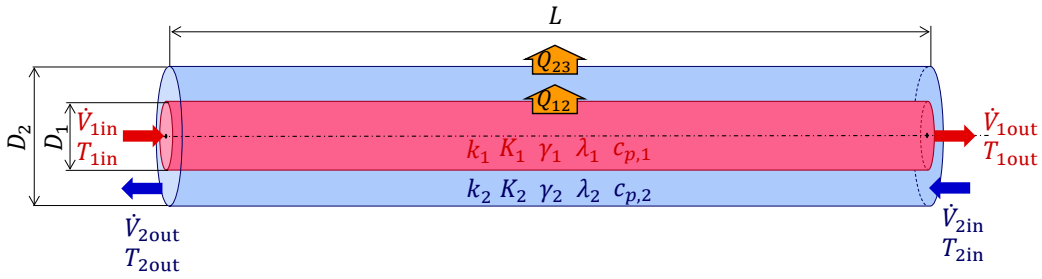

Figure 2. Counterflow double-pipe heat exchanger model.

2.2. Plug-Flow Reactor Model

In this study, we assumed an absence of concentration or temperature gradients in the radial direction of each pipe. Hence, we modeled the system using a one-dimensional plug-flow reactor (PFR) from the open-source Cantera library, which was developed for detailed chemical reaction calculations. This model is suitable when variations only occur along the flow path from the inlet to the outlet of the reactor. The PFR model in this study was longitudinally divided into cells with a width of Δx, as illustrated in Figure 3, and the simulation cells were integrated to replicate a one-dimensional flow for the reaction calculations [38]. The properties of each cell were computed using Cantera's Ideal Gas Reactor feature. The basic equation for the PFR, substituting the effect of heat transfer for the quantity of heat Qin (obtained in Section 3) received by the cell through heat exchange with a high-temperature heat source and converging it with the Newton–Raphson method, is as follows:

$$mc_v \frac{dT}{dt} = -p\frac{dV}{dt} + Q + \sum_{\text{up}} \dot{m}_{\text{up}} \left(H_{\text{up}} - \sum_k U_k Y_{k,\text{up}} \right) - \frac{pV}{m} \sum_{\text{down}} \dot{m}_{\text{down}} - \sum_k \dot{m}_{k,\text{gen}} U_k, \quad (2)$$

where $\dot{m}$ is the mass flow rate of species into the seed cell per unit time, H_{up} is the total enthalpy of cell, U_k is the total internal energy, V is the volume of the cell, c_v is the specific heat of the mixture, Y_k is the mass fraction of each generated species, and T is the cell temperature. The subscript up is the inflow to the cell, while down is the outflow from the cell, the subscript k is the chemical species, and gen is the generation in the cell. For detailed calculations regarding the PFR methodology, please refer to [38]. The solution is closed in the equation of state; see reference [38] for the equation of state.

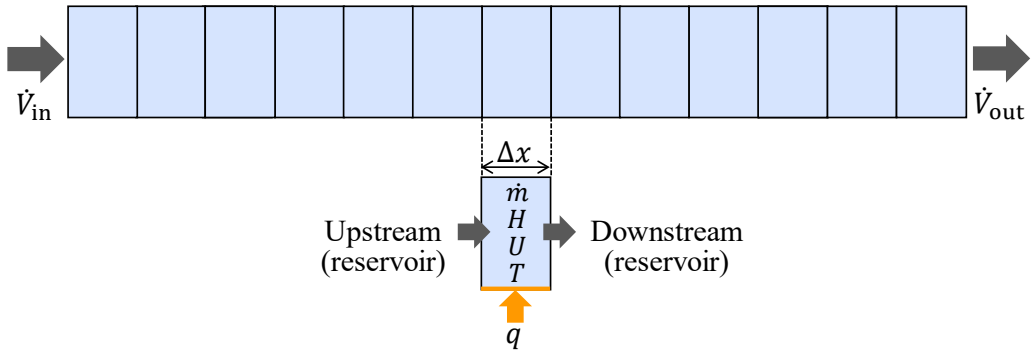

Figure 3. Plug-flow reactor (PFR) model.

2.3. Theory of the Counterflow Double-Pipe Heat Exchanger

The symbols for the various quantities considered in the heat transfer simulation are defined in Figure 2.

$$Q_{12} = K_{12}(T_1 - T_2), \quad (3)$$

where T_1 is the temperature of the fluid in the inner pipe and T_2 is the temperature of the fluid in the outer pipe. The overall heat transfer coefficient K_{12} between the inner and outer pipes is expressed as follows:

$$K_{12} = \frac{1}{\left(\frac{1}{K_1}\right) + \gamma_1 + \left(\frac{\delta}{k}\right) + \gamma_2 + \left(\frac{1}{K_2}\right)}, \tag{4}$$

where γ_1 and γ_2 are the fouling coefficients of the inner and outer tubes, respectively. In this study, the surface was considered smooth, and the stain coefficient was set to 0. δ is the pipe thickness, k_1 and k_2 are the thermal conductivity of the inner and outer pipe, respectively, and K_1 and K_2 are the heat transfer coefficients between the inner and outer fluids, respectively, and the pipe wall. The relationships between the Nusselt number Nu and K_1 and K_2 are given by

$$K_1 = \frac{Nu_1 \lambda_1}{D_1}, \tag{5}$$

$$K_2 = \frac{Nu_2 \lambda_2}{D_2}, \tag{6}$$

where λ denotes the thermal conductivity of the fluid, and temperature dependence is also considered. Because the simulation system used a double-pipe configuration, the effective pipe diameter D_{eff2} is calculated as follows:

$$D_{\text{eff2}} = 4\frac{\frac{\pi}{4}\left({D_2}^2 - {D_1}^2\right)}{\pi(D_2 + D_1)}, \tag{7}$$

where D_2 and D_1 are the actual outer and inner pipe diameters, respectively.

Owing to the change in temperature and chemical reactions, the physical properties vary inside the pipe, influencing the heat transfer coefficient. Therefore, Nu was determined using the Hausen equation under laminar conditions (with a Reynolds number $Re < 2300$) as follows:

$$Nu_i = 3.66 + \frac{0.068\left(Re_i \times Pr_i \times \frac{D_i}{L}\right)}{1 + 0.04\left(Re_i \times Pr_i \times \frac{D_i}{L}\right)^{\frac{2}{3}}}, \tag{8}$$

where D_{eff2} and D_1 represent the diameters of the outer and inner pipes, respectively. The subscripts eff2 and i (assigned as 1) indicate the outer and inner pipes, respectively. For turbulent conditions ($Re > 2300$), the Colburn equation was employed as follows:

$$Nu_i = 0.023 \times {Re_i}^{\frac{4}{5}} \times {Pr_i}^{\frac{1}{3}}, \tag{9}$$

where Re can be calculated using the fluid density ρ, fluid velocity v, pipe diameter D, and fluid viscosity μ as follows:

$$Re_i = \frac{\rho_i v_i D_i}{\mu_i}. \tag{10}$$

Equations (8)–(10) are calculated based on the physical properties of the outer and inner pipes obtained from the state equations in [38].

The Prandtl number Pr is obtained using the specific heat C_p, viscosity coefficient μ, and thermal conductivity k as follows:

$$Pr_i = \frac{C_{pi}\mu_i}{k_i}. \tag{11}$$

Pr is calculated based on the physical properties of the outer and inner pipes, obtained from the equation of state. The equation of state and Reynolds number can be found in reference [38].

Because the heat transfer between the outer pipe and the external environment must be considered, this study calculated the heat transfer to the external environment Q_{23} using the external heat transfer coefficient K_{23} and external ambient temperature T_3 as follows:

$$Q_{23} = K_{23}(T_2 - T_3), \tag{12}$$

where K_{23} is calculated in the same manner as Equation (4).

2.4. Programmatic Association

In Cantera, a reactor (a single cell) was treated as having an inlet and outlet connecting it in series with other reactors. Thus, the calculations proceeded sequentially from the upstream to the downstream end of each pipe. However, the direct simulation of heat transfer between the inner and outer pipes in a counterflow double-pipe configuration is infeasible in a typical one-dimensional model. Hence, a modified approach was used to simulate heat transfer in which the inner and outer pipes were simulated as coupled PFRs, as depicted in Figure 4.

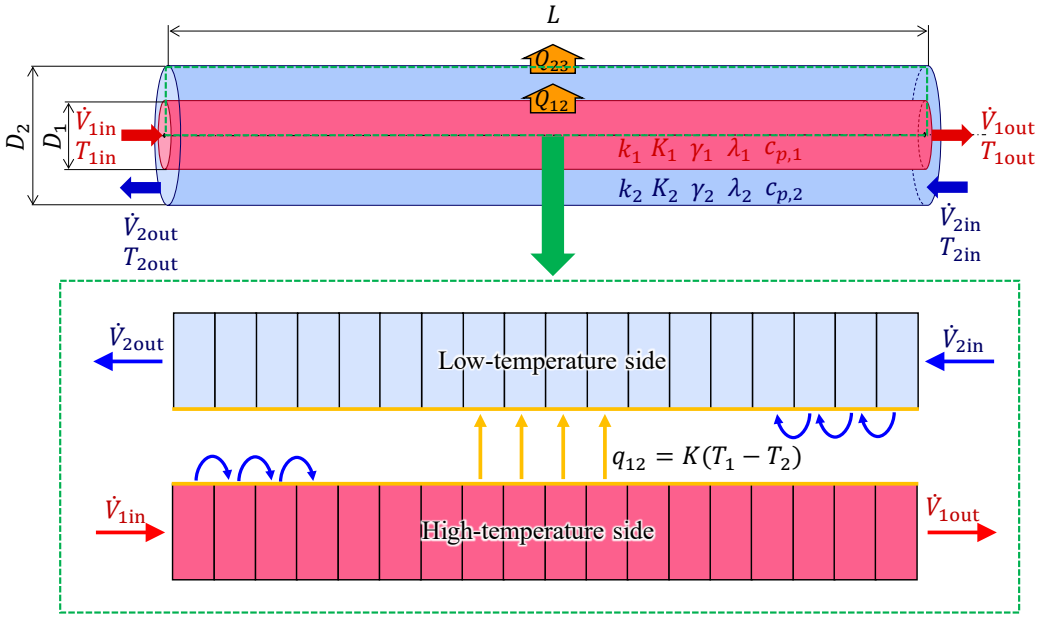

Figure 4. Coupled PFR models considering counterflow.

The heat transfer Q_{12} between the inner and outer pipes can be calculated as follows:

$$Q_{12} = K_{12}(T_1 - T_2) \tag{13}$$

where K is the overall heat transfer coefficient, T_1 is the inner pipe temperature, and T_2 is the outer pipe temperature.

This approach enables the simulation of heat transfer between the inner and outer pipes by coupling PFRs that replicate their behaviors.

The two PFRs were solved sequentially from their upstream ends while considering the heat exchange between the inner and outer pipes as well as the effects of the chemical reactions. The primary focuses of this calculation are the chemical reactions, fluid flow, and heat conduction. Considering the small diameter of the pipes in this study, the effects of diffusion, such as concentration distribution and thermal diffusion (temperature distribution), were deemed negligible and disregarded. In addition, we assumed the absence of a radial temperature distribution, allowing us to neglect multidimensional flow effects. Consequently, calculations could be performed from upstream to downstream without considering the downstream effects.

As shown in the lower part of Figure 4, the PFRs modeling the inner and outer pipes were arranged in series. The simulation proceeded by sequentially solving the corresponding cells of each pipe and calculating the heat exchange between them. This computational procedure was implemented using the following iterative method:

1. Calculate the temperature in the PFR on the high-temperature side while maintaining a constant temperature in the PFR on the low-temperature side.
2. Calculate the temperature in the PFR on the low-temperature side while maintaining the temperature in the PFR on the high-temperature side at the value obtained in Step 1, and compute the heat transfer.
3. Recalculate the temperature in the PFR on the high-temperature side while maintaining the temperature in the PFR on the low-temperature side at the value obtained in Step 2, and compute the heat transfer.
4. Recalculate the temperature in the PFR on the low-temperature side while maintaining the temperature in the PFR on the high-temperature side at the value obtained in Step 3, and compute the heat transfer.
5. Repeat Steps 3 and 4 until the convergence criteria presented in Section 2.5 are satisfied.

2.5. Convergence Criteria

For the iterative calculation of heat transfer between coupled PFRs, convergence was determined using the squared error between the relevant physical quantities at the exit of the inner pipe in successive iterations as follows:

$$error = \sqrt{\Sigma(\varnothing_n - \varnothing_{n-1})^2}, \tag{14}$$

where $\varnothing$ is the selected physical quantity being assessed and n is the iteration number. As this investigation focused on hydrogen concentration, the convergence assessment employed the temperature $T_{1\text{out}}$ and hydrogen mole fraction $X_{H_2\_2\text{out}}$ at the exit of the inner pipe as $\varnothing$ values. Convergence was considered achieved when the *error* calculated using Equation (14) fell below the specified threshold—set to 10^{-3}.

3. Numerical Analysis

This section presents the numerical analysis of the proposed combustion-heated methane pyrolysis system shown in Figure 1. This analysis considered hydrogen combustion and methane pyrolysis, for which calculations were performed using the counterflow double-pipe heat exchanger introduced in Section 2.4. The conditions under which independent system operation was possible were evaluated by comparing the inflow of hydrogen fuel at the inlet of the inner pipe with the outflow of produced hydrogen at the outlet of the outer pipe and calculating the amount of remaining hydrogen as the product. These conditions were defined using the following relationship:

$$\dot{V}_{H_2\_\text{prod.}} = (2\alpha - \beta)\dot{V}_{1\text{in\_CH}_4}, \tag{15}$$

where $\dot{V}_{H_2\_\text{prod.}}$ is the generated hydrogen flow rate, $\dot{V}_{1\text{in\_CH}_4}$ is the methane inflow rate, α is the methane conversion rate, and β is the hydrogen combustion rate; system feasibility was confirmed when $\dot{V}_{H_2\_\text{prod.}}$ was greater than 0. Methane conversion α is also a measure of the degree of change in a particular chemical substance induced by a reaction in a chemical process or reaction and an indicator of the rate of change from methane (before the reaction) to the product (after the reaction). $\dot{V}_{1\text{in\_CH}_4}$ and β are user-set as calculation conditions.

In this analysis, Shimizu's detailed reaction model [39] was used for hydrogen combustion, and the Ranzi-based model [40] developed in our previous work [41] was used for methane pyrolysis.

3.1. Determining Basic Model Configuration

The thermal decomposition of methane is considered a moderately endothermic reaction. Non-catalytic methane thermal decomposition reactions generally require high-temperature conditions given the strength of the C-H bonds [30,35,42–48]. Methane begins to decompose and produce a small percentage of hydrogen at temperatures at or above approximately 1000–1100 °C [30,35,45–48]. Furthermore, it has been suggested that methane is almost entirely decomposed at temperatures at or above approximately 1150 °C, corresponding to a hydrogen yield of approximately 0.85–0.97 [35,42–44,47,48]. Therefore, we conducted heat transfer and reaction analyses to determine the basic configuration of the counterflow double-pipe heat exchanger capable of achieving a target temperature of 1200 °C considering a high-temperature T_2 fluid in the inner pipe and low-temperature fluid T_1 in the outer pipe. The heat exchanger was modeled using the method described in Section 2 with the geometry shown in Figure 2. The pipe length L was estimated without considering heat exchange with the surrounding environment. The calculation conditions for these analyses are listed in Table 1. The subscripts 1 and 2 represent the inner and outer tubes, respectively, and the subscripts in and out represent the inflow and outflow into and out of the tubes, respectively.

Table 1. Calculation conditions to determine basic model configuration.

Conditions	Parameters	Set Value
Geometry conditions	Inner pipe diameter, D_1	20 mm
	Outer pipe diameter, D_2	40 mm
	Double-pipe length, L	3 m
Flow rate conditions	Methane flow rate, $\dot{V}_{2in\_CH_4}$	2.55 L/min
	Combustion hydrogen flow rate, $\dot{V}_{1in\_H_2}$	1.7 L/min
	Equivalence ratio, φ	1.0
	Oxidizing agent	Air
	Pressure, p	101,325 Pa

Figure 5 illustrates the results of these analyses: Figure 5a depicts the counterflow double-pipe heat exchanger model used in the calculations, with the left end set at 0 m and the right end set at 3 m, Figure 5b presents the results of hydrogen combustion in the inner pipe, and Figure 5c shows the thermal decomposition of methane within the outer pipe. The gas flow directions are indicated by the arrows in the respective diagrams.

This calculation treated the system as an adiabatic container without considering any heat exchange with the surroundings. However, the combustion hydrogen temperature results in Figure 5b suggest that heat exchange occurred between the inner and outer pipe. Additionally, the gradual temperature gradient observed in the regions circled in green in Figure 5c suggests that an endothermic reaction occurred. Because only methane flowed through the outer pipe, we can assume that the thermal decomposition reaction of methane described in Equation (1) began at approximately 1.4 m. The temperature of methane gas at this location was approximately 1000–1100 °C, which is consistent with the experimental data on gas-phase methane thermal decomposition found in the literature [30,35,45–48]. Furthermore, the target temperature of 1200 °C was achieved at 2.5 m from the methane inlet in the outer pipe. The results indicate that, under the conditions of this study, a length of approximately 3.0 m is required to achieve the desired target heating temperature of 1200 °C and achieve methane pyrolysis without the use of a catalyst.

In terms of system feasibility, Figure 5 shows that under the conditions outlined in Table 1, the value of α was 0.59, and the value of β was 0.67; thus, according to Equation (15), $\dot{V}_{H_2\_prod.}$ = 1.30 L/min, satisfying the system feasibility condition of $\dot{V}_{H_2\_prod.} > 0$. The purpose of this study was to investigate the technical feasibility of a hydrogen production process and to determine optimal flow conditions. Therefore, the basic configuration

evaluated in this study employed a 3.0 m long heat exchanger. The methane inflow conditions ($\dot{V}_{2in\_CH_4}$ =2.55 L/min) in this section also identified the upper and lower process limits of β as 1.6 and 0.4, respectively, at the combustion flow rate; these details are discussed in Section 3.2.

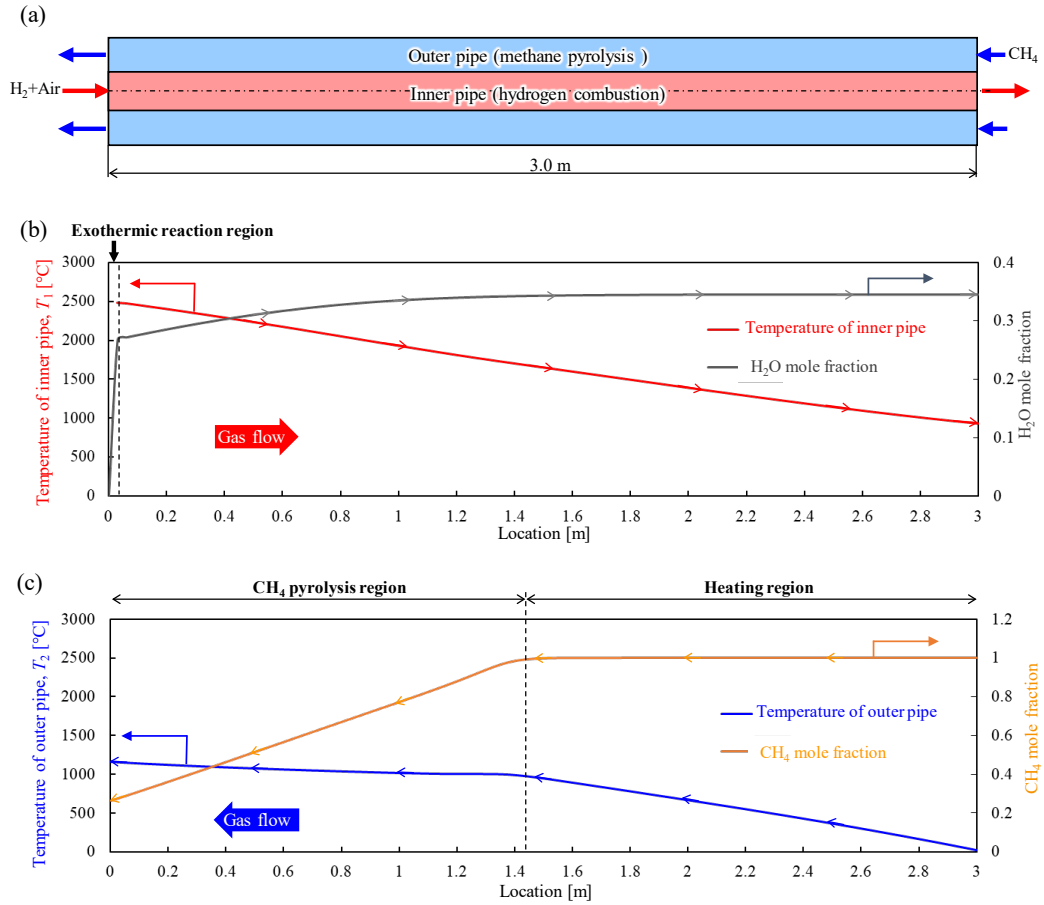

Figure 5. Determining the basic system configuration: (**a**) system model; (**b**) gas flow characteristics in the inner pipe (red: temperature; gray: H_2O mole fraction); (**c**) gas flow characteristics in the outer pipe (blue: temperature; orange: CH_4 mole fraction).

3.2. System Investigations

This section describes the calculations conducted to investigate the characteristics of the system under various flow conditions. These calculations were achieved by varying the hydrogen flow rate for combustion $\dot{V}_{1in\_H_2}$ in the inner pipe and the methane flow rate $\dot{V}_{2in\_CH_4}$ in the outer pipe utilizing the basic model configuration obtained in Section 3.1. The calculation conditions employed during this analysis are listed in Table 2.

Table 2. Calculation conditions to conduct system investigations.

Conditions	Parameters	Set Value
Geometry conditions	Inner pipe diameter, D_1	20 mm
	Outer pipe diameter, D_2	40 mm
	Double-pipe length, L	3.0 m
Flow rate conditions	Methane flow rate, $\dot{V}_{2in\_CH_4}$	1.5–5.0 L/min
	Combustion hydrogen flow rate, $\dot{V}_{1in\_H_2}$	1.0–10.0 L/min
	Equivalence ratio, φ	1.0
	Oxidizing agent	Air
	Pressure, p	101,325 Pa

3.2.1. General System Performance

Figure 6 depicts the general system performance according to the hydrogen flow rate $\dot{V}_{1in\_H_2}$ and methane flow rate $\dot{V}_{2in\_CH_4}$. The conditions under which the generated hydrogen flow rate satisfied the system feasibility condition ($\dot{V}_{H_2\_prod.} > 0$), indicating system independence, are enclosed by the red lines. These results indicate the combustion conditions under which the system is feasible and inform the estimation of the conditions required for maximum hydrogen production within the considered ranges. The hydrogen production levels depicted in Figure 6 increase with the methane flow rate until the maximum hydrogen production is achieved at a methane flow rate of 10 L/min, after which hydrogen production begins to decrease. Thus, the optimal conditions were achieved when both the methane and combustion hydrogen flow rates were 10 L/min, resulting in a hydrogen production rate of 2.7 L/min (calculated using Equation (15)).

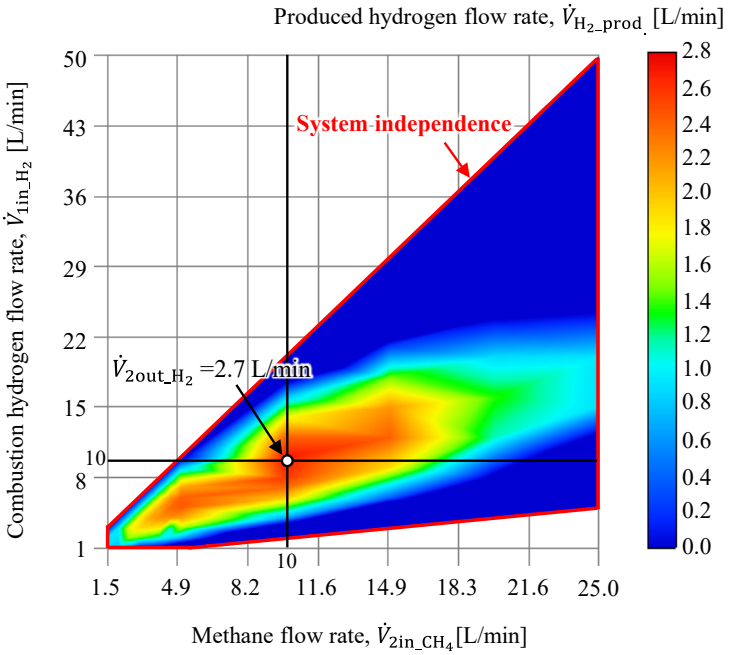

Figure 6. Produced hydrogen flow rate ($\dot{V}_{H_2\_prod}$) according to methane and combustion hydrogen flow rates ($\dot{V}_{2out\_CH_4}$, $\dot{V}_{1in\_H_2}$).

A detailed analysis of the changes in Figure 6 is shown in Figure 7, which presents the outer pipe temperature T, velocity v, residence time τ, and mole fraction of methane X_{CH_4} obtained when varying the methane flow rate $\dot{V}_{2in\_CH_4}$ (5, 10, and 25 L/min) while maintaining a constant combustion hydrogen flow rate $\dot{V}_{1in\_H_2}$ of 10 L/min. The residence time τ was calculated as

$$\tau = \frac{\frac{\pi}{4} \times (D_2 - D_1)^2 \times L}{\dot{V}_{2in\_CH_4}}, \quad (16)$$

where D_1 and D_2 are the inner and outer diameters, respectively. L is the length of the pipe. $\dot{V}_{2in\_CH_4}$ is the flow rate of the gas flowing into the outer tube, that is, the flow rate of methane of the raw material in hydrogen production. Because the residence time τ is inversely proportional to the flow rate, a decrease in the residence time is considered to have limited methane gas heating, hindering the reaction. This is consistent with other findings in the literature [49–52], which reported that an increase in residence time τ consistently led to higher hydrogen yields across all temperature conditions. Therefore, under the conditions applied in this study, which were primarily related to the model geometry, a minimum residence time of at least 3.0 s was required.

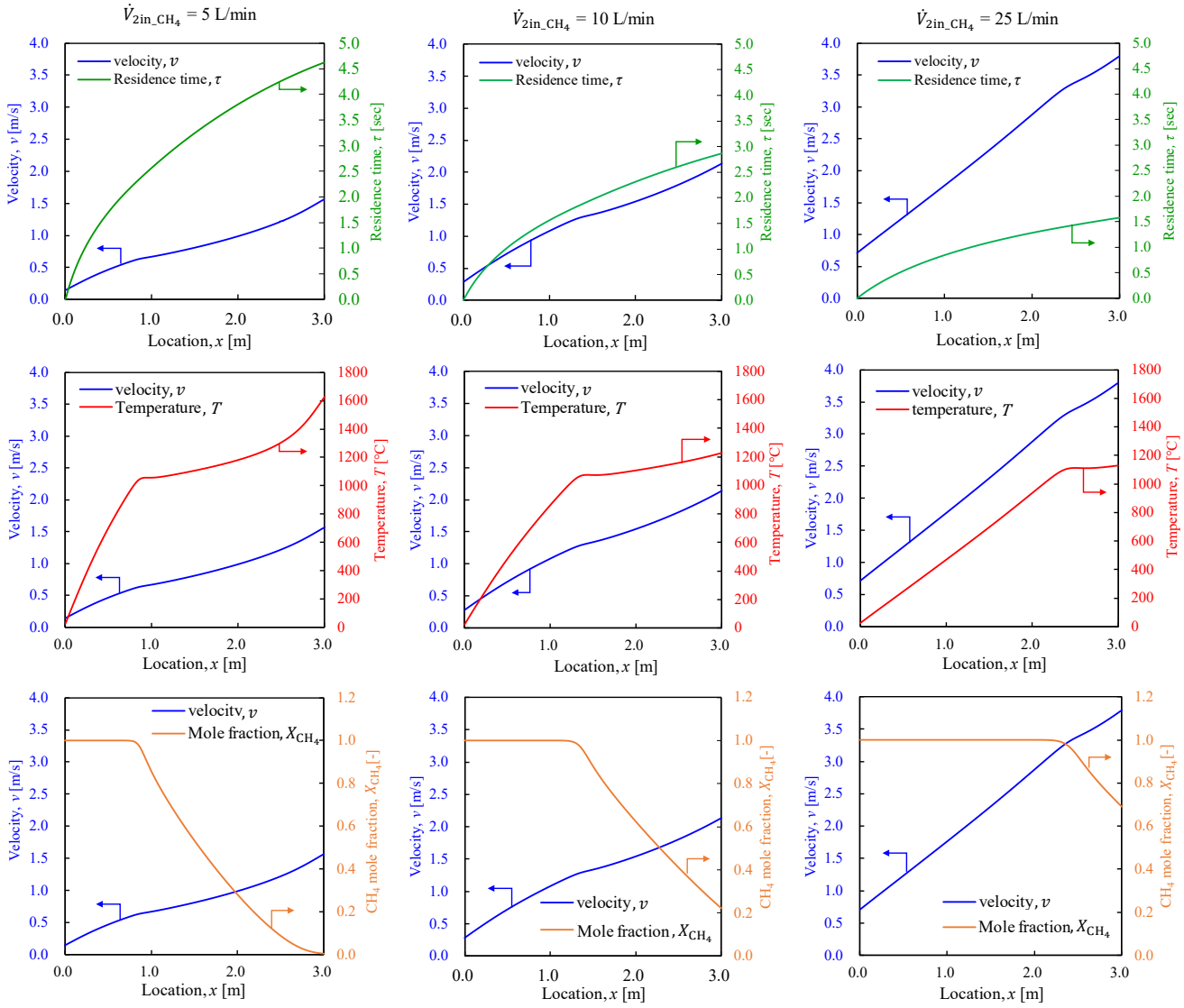

Figure 7. Characteristic results in the inner part of the outer pipe under methane flow rates ($\dot{V}_{2in\_CH_4}$) of 5, 10, and 25 L/min.

To the right of the line in Figure 6 representing the condition for maximum hydrogen production (a methane flow rate of 10 L/min), increasing the methane flow rate clearly led to an increase in hydrogen production; to the left of the line, the reduction in residence time had a significant effect on hydrogen production. In the region above the line representing the condition for maximum hydrogen production (a hydrogen flow rate of 10 L/min), an increase in the recovered hydrogen β consumed by combustion decreased the overall hydrogen yield from the system; in the region below the line, a decrease in recovered hydrogen β consumed by combustion led to a decrease in thermal energy, preventing the attainment of the 1200 °C target heating temperature and resulting in a less favorable reaction with reduced hydrogen production.

Figure 8 shows the simulated methane conversion rate α, indicating that under the conditions yielding the maximum hydrogen production rate shown in Figure 6, the methane conversion rate α was approximately 60%. Thus, the proposed system must employ a separator to separate methane and hydrogen, as a high concentration of hydrogen is necessary to reduce energy costs in practical applications. Furthermore, the combustion of 1 mol of methane results in the emission of 1 mol of carbon dioxide; therefore, an improvement in the methane conversion rate α is expected to lead to a proportional reduction in carbon dioxide emissions. Additionally, as the hydrogen used in fuel cells must

have a minimum purity of 99.97%, the conditions that yield the highest concentrations of hydrogen must be investigated. Figure 6 clearly indicates that high hydrogen concentrations were achieved over a wide range toward the lower end of the considered methane flow rate range. This likely occurred owing to the adequate heating of methane gas with increased residence time τ, which promoted the reaction. Indeed, the top row of Figure 7 shows that an increase in the flow rate $\dot{V}_{2in\_CH_4}$ led to a decrease in the residence time τ, which is confirmed by Equation (16). Therefore, a decrease in residence time τ significantly contributes to a decrease in the methane conversion rate α. Focusing on the middle and bottom rows in Figure 7, the velocity v increased linearly before changing to increase gradually in a quadratic manner. The point of transition between these behaviors aligns with the initiation of methane thermal decomposition, as indicated by the temperature and CH_4 mole fraction results. The linear increase in the flow rate reflects the characteristics of thermal expansion owing to methane heating through heat exchange, whereas the quadratic increase is believed to be influenced by the increase in the number of moles owing to methane thermal decomposition reactions. This suggests that methane thermal decomposition reactions occur not only from the results of the methane mole fraction but also from the changes in velocity v.

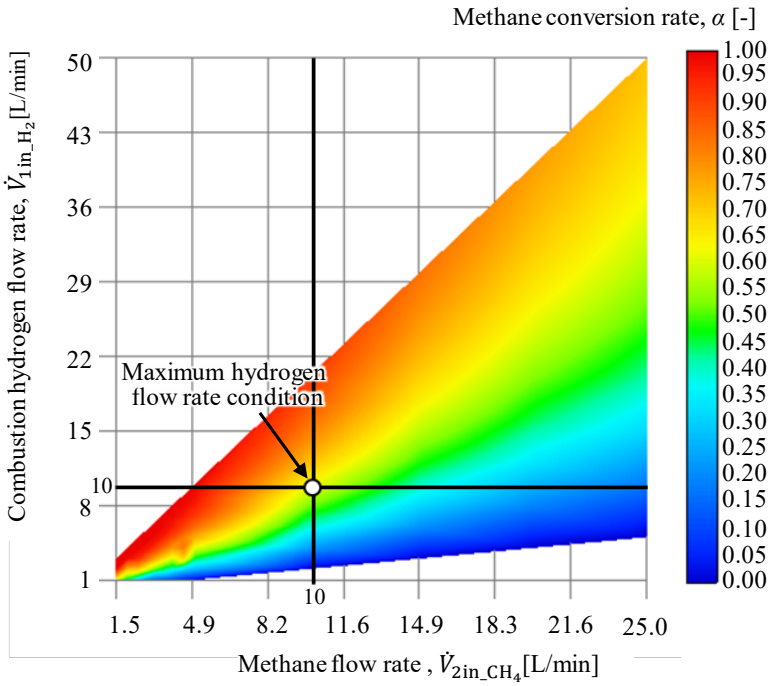

Figure 8. Methane conversion rate (α) according to methane and combustion hydrogen flow rates ($\dot{V}_{2out\_CH_4}$, $\dot{V}_{1in\_H_2}$).

Figure 8 also indicates that a hydrogen concentration greater than 80% was widely achieved with a higher combustion hydrogen flow rate $\dot{V}_{1in\_H_2}$. Figure 9 accordingly presents the outer pipe temperature T, velocity v, residence time τ, and mole fraction of methane $X_{2out\_CH_4}$ obtained when varying the combustion hydrogen flow rate $\dot{V}_{1in\_H_2}$ (4 and 7 L/min) and maintaining a constant methane flow rate $\dot{V}_{2in\_CH_4}$. Notably, the temperatures T reported in the middle row of Figure 9 indicate that a higher combustion hydrogen flow rate corresponded to a more rapid increase in temperature along the pipe. This was likely a result of the higher hydrogen combustion heat input from the inner pipe, which caused the temperature to increase and led to a higher degree of methane decomposition. This increased the number of moles in the outer pipe under the same methane flow rate $\dot{V}_{2in\_CH_4}$, consequently increasing the velocity v of the outer pipe, resulting in varying residence times τ.

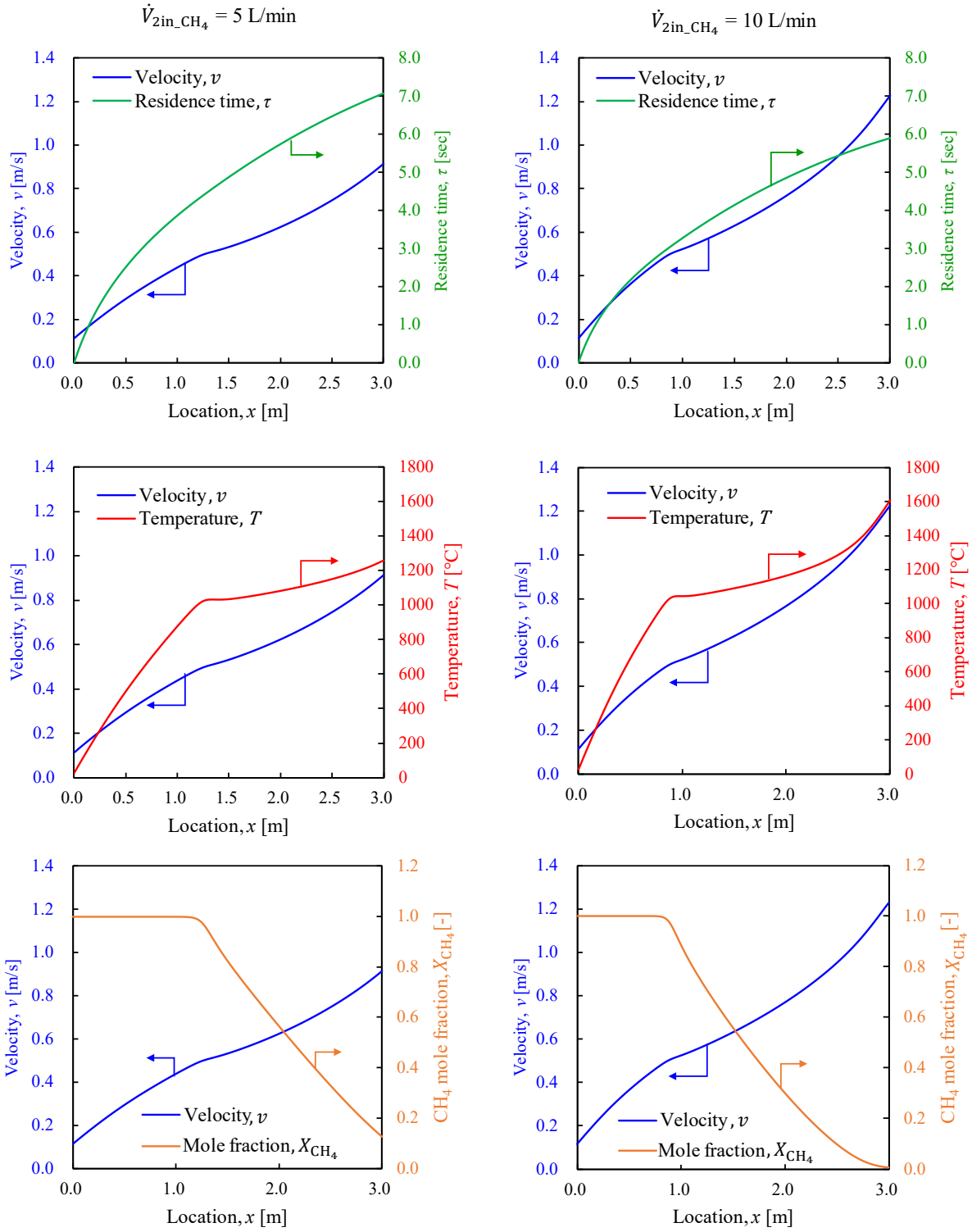

Figure 9. Characteristic results of the inner part of the outer pipe under combustion hydrogen flow rates ($\dot{V}_{1in\_H_2}$) of 4 and 7 L/min.

These observations suggest that residence time τ plays a critical role in the methane conversion rate $\dot{V}_{2in\_CH_4}$ when varying the methane flow rate and that conditions with increased heat input from the inner pipe can enhance the methane conversion rate α. Additionally, the findings presented in Figures 6 and 8 offer valuable insights when estimating the suitable conditions for various applications of the proposed hydrogen generation system.

3.2.2. Outer Pipe Temperature

Next, we evaluated the ability of the proposed system to achieve the target temperature of 1200 °C in the outer pipe. The results are presented in Figure 10 in terms of the distance from the outer pipe inlet, with shorter distances indicating a wider region above 1200 °C. The figure indicates that a lower methane conversion rate is a result of the limited region in which the target heating temperature is exceeded, and therefore, more of the pipe is less conducive for reactions. This suggests that hydrogen production can be increased by extending the residence time, expanding the distance over which heat exchange occurs, and improving the heat exchange efficiency through changes in the system design.

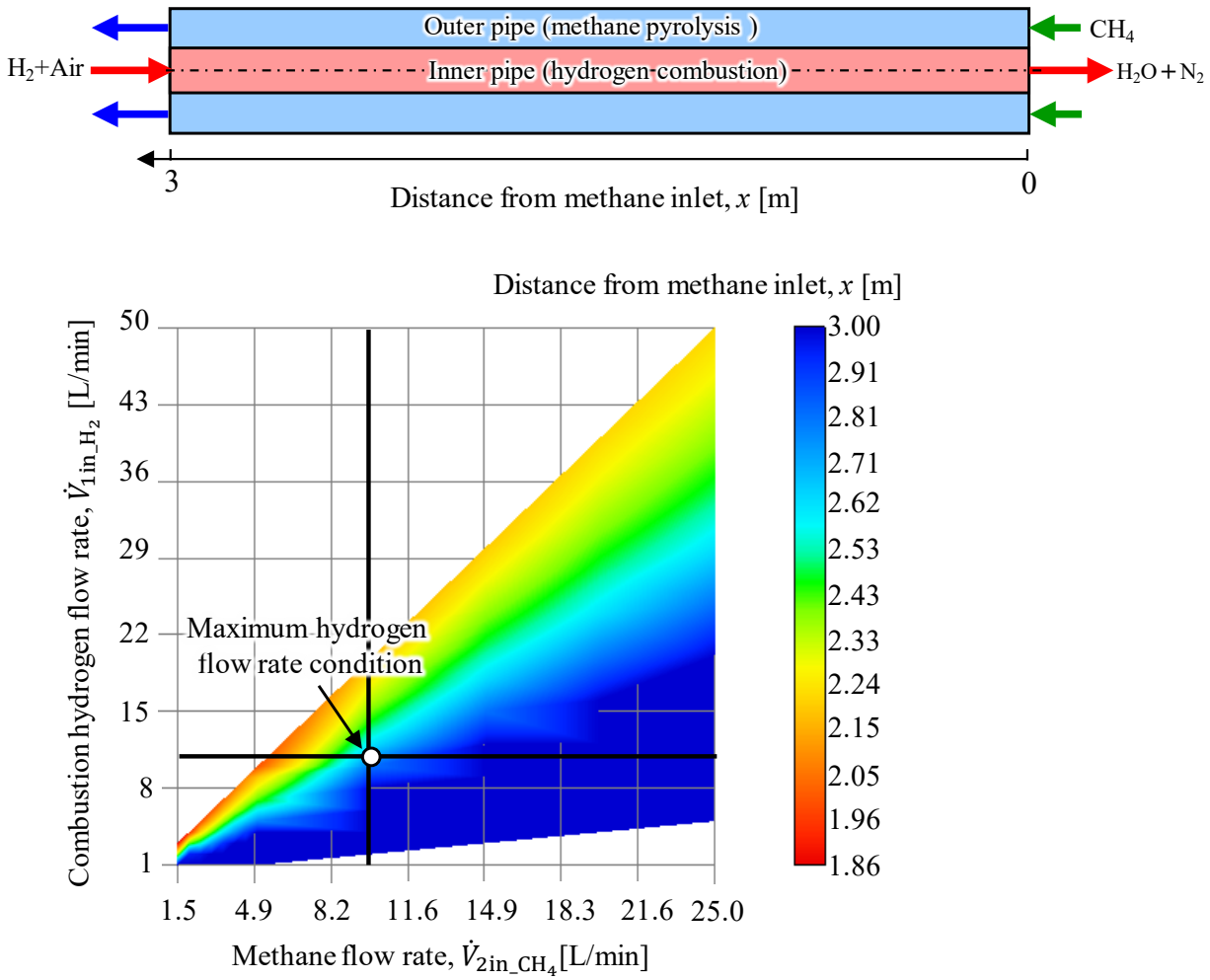

Figure 10. Locations (x) at which 1200 °C is achieved in the outer pipe.

Figure 11 shows the temperature distributions obtained under combustion hydrogen flow rates $\dot{V}_{1in\_H_2}$ of 2, 10, and 20 L/min, while the methane flow rate $\dot{V}_{2in\_CH_4}$ was held constant. The region enclosed by the green circle exhibits a gradual temperature gradient, suggesting the occurrence of endothermic reactions such as methane pyrolysis; the region enclosed by the red circle displays a steeper temperature gradient, indicating that these reactions were completed. Under the highest combustion hydrogen flow rate, much of the pipe length was wasted owing to the early completion of the reactions, whereas under the other two flow rates, the target temperature was not achieved, indicating insufficient heat exchange and inadequate pipe length. Thus, these results confirm that optimal conditions exist for each parameter.

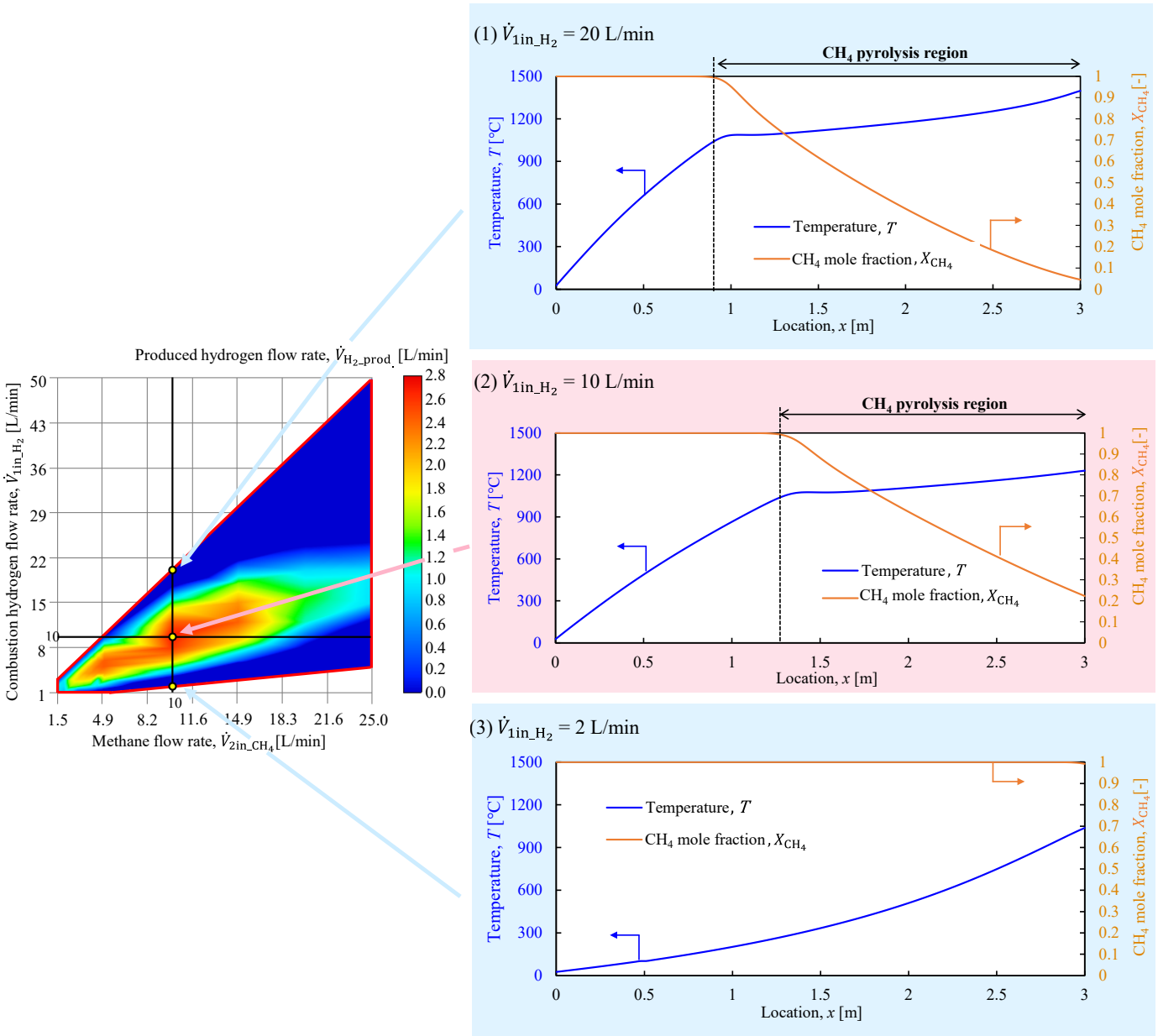

Figure 11. Temperature (T) distributions in the outer pipe under combustion hydrogen flow rates ($\dot{V}_{1in\_H_2}$) of 2, 10, and 20 L/min.

3.2.3. System Efficiency

The energy efficiency of hydrogen production in the system η_{H_2} was determined as follows:

$$\eta_{H_2} = \frac{\dot{m}_{p-H_2} \Delta q_{H_2}}{\dot{m}_{r-CH_4} \Delta q_{CH_4}}, \quad (17)$$

where $\dot{m}_{p-H_2}$ is the mass flow rate of hydrogen at the outlet, $\dot{m}_{r-CH_4}$ is the mass flow rate of methane at the inlet, Δq_{H_2} is the higher heating value of hydrogen, and Δq_{CH_4} is the higher heating value of methane.

Figure 12 illustrates the system efficiency for the area enclosed by the red frame in Figure 1. The maximum efficiency achieved under the conditions considered in this study was 30%. Furthermore, the system exhibited higher efficiency at lower flow rates for both methane and combustion hydrogen owing to the associated elevated methane conversion rate, as illustrated in Figure 8, leading to the production of a larger quantity

of hydrogen. Finally, the reduced consumption of combustion hydrogen led to a higher hydrogen content in the product. Consequently, the system efficiency is expected to be higher under low-flow conditions.

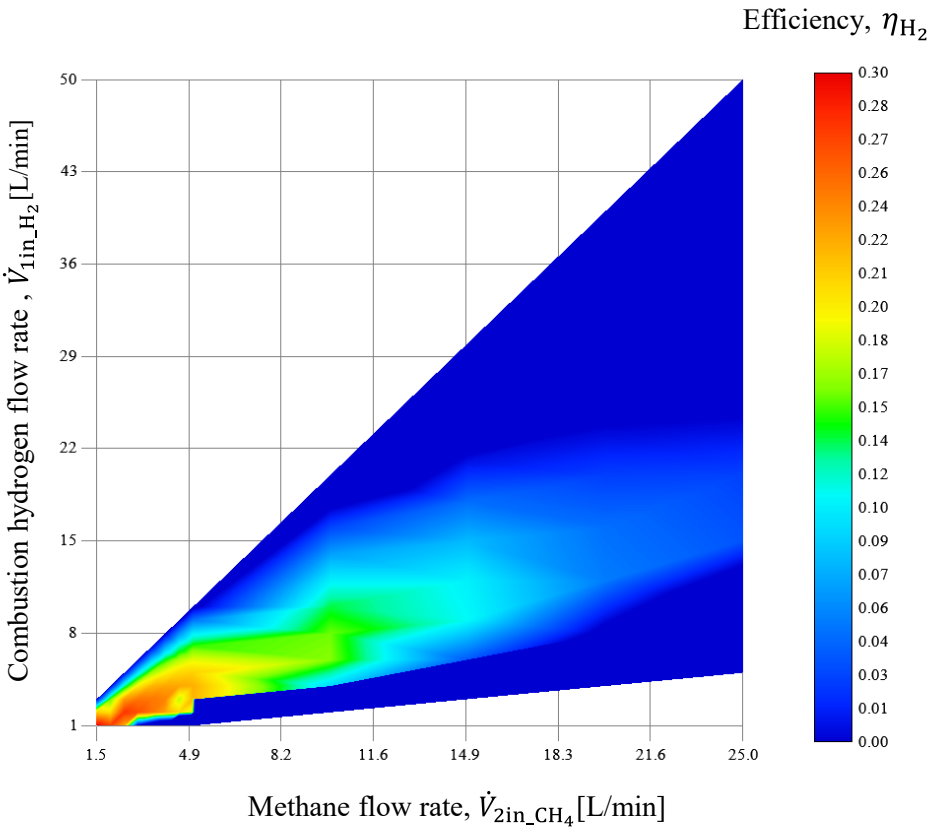

Figure 12. System efficiency map (product: hydrogen).

Similar to Equation (17), the energy efficiency of hydrogen and carbon production when considering both hydrogen and carbon as products was determined as follows:

$$\eta_{H_2,C} = \frac{\dot{m}_{p-H_2}\Delta q_{H_2} + \dot{m}_{p-C}\Delta q_C}{\dot{m}_{r-CH_4}\Delta q_{CH_4}}, \quad (18)$$

where $\dot{m}_{p-C}$ is the mass flow rate of carbon at the outlet and Δq_C is the higher heating value of carbon.

Figure 13 shows the system efficiency when considering the co-production of hydrogen and carbon, indicating similar results to the methane conversion rate map in Figure 8. This correlation can be attributed to the fact that carbon, unlike hydrogen, is not reclaimed within the system, leading to outcomes that directly correspond to the methane conversion rate. This implies that carbon exerts a more significant influence on the system efficiency than hydrogen when both are considered products. Moreover, when carbon is considered a product, the maximum system efficiency approaches approximately 55%, indicating the potential for substantial enhancement. Because the sale of generated carbon for use in various commercial applications could help to reduce the market price of hydrogen, further investigation of the carbon produced from methane pyrolysis and carbon capture technologies is recommended.

The hydrogen production and methane conversion rates presented in Section 3.2.1 and the system efficiency results discussed in this section suggest that investigations should focus on the lower range of methane flow rates to capitalize on the corresponding relatively high methane conversion rates and determine the conditions that optimize hydrogen production.

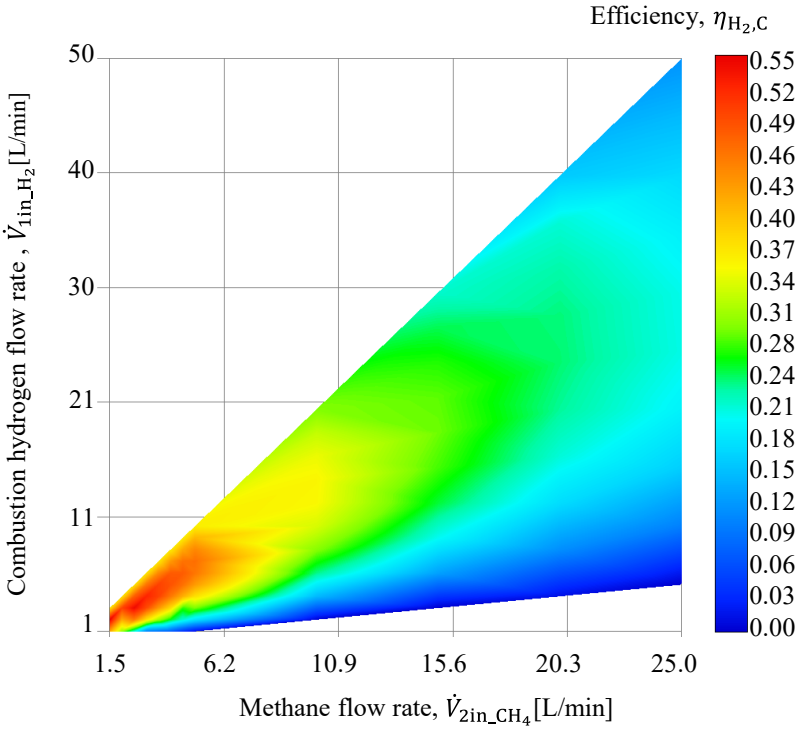

Figure 13. System efficiency map (products: hydrogen and carbon).

4. Conclusions

The production of hydrogen by methane pyrolysis has been extensively investigated through both experiments and numerical analyses. However, many previously proposed methane pyrolysis methods involve the use of catalysts or electrical heating, which often incur significant financial costs. Therefore, a novel methane pyrolysis hydrogen production system in which a portion of the generated hydrogen is used for combustion to heat the methane was developed. In addition to detailed chemical reaction calculations, we created a computational environment for the proposed counterflow double-pipe heat exchanger utilizing a coupled PFR model to numerically simulate heat transfer between the inner and outer pipes. The following conclusions were drawn from the results of this study:

- An investigation of the fundamental geometry of a counterflow double-pipe heat exchanger was conducted using the PFR-based model. The results indicate that under the conditions of this study, a length of approximately 3.0 m is required to achieve the desired target heating temperature of 1200 °C and achieve methane pyrolysis without the use of a catalyst. Furthermore, this configuration met the feasibility criteria for the proposed system under the considered conditions.
- The base configuration applied in this study was applied to explore the system viability by varying the methane and combustion hydrogen flow rates to determine the conditions for achieving the maximum produced hydrogen flow rate. The results indicate that given the considered study configuration, a minimum methane residence time of at least 3.0 s is required.
- The methane conversion rate map revealed a methane conversion rate of approximately 60% at the point where hydrogen production was maximized. The methane conversion rate increased as the methane flow rate decreased and the combustion hydrogen flow rate increased. Thus, the residence time and conditions that allow greater heat transfer from the inner pipe to the outer pipe were identified as significant contributors to higher methane conversion rates.
- Methane conversion and hydrogen production maps were obtained to provide an index for estimating the system conditions according to the desired hydrogen generation application.

- The flow conditions investigated in this study confirmed that the optimal conditions were a methane flow rate of 10 L/min and a combustion hydrogen flow rate of 10 L/min (β = 1.0), at which the methane conversion was α = 0.64 and the product hydrogen flow rate was 2.7 L/min.
- By focusing on the temperature of the methane gas in the outer pipe, an optimal configuration was observed for each set of conditions, suggesting that increasing the residence time, enhancing the heat exchange distance, and improving the heat exchange efficiency through modifications in the pipe geometry, such as increasing the inner tube diameter and attaching fins to the inner tube to enlarge the heat transfer surface area, can improve hydrogen production.
- An investigation of system efficiency produced a map indicating higher efficiency at lower methane flow rates. Furthermore, system efficiency improved when carbon was considered as a product, suggesting that carbon also has a significant impact on system efficiency and indicating the necessity of further investigations into the production of carbon by methane pyrolysis.

This study successfully demonstrated the feasibility of a novel combustion-heated methane pyrolysis hydrogen production system in which a portion of the generated hydrogen is used to heat the methane. This system provides an environmentally friendly and cost-effective approach to hydrogen production. Our findings indicate the potential for increased hydrogen production at reduced cost owing to the ability to utilize generated carbon, suggesting that the proposed system provides an effective method for future hydrogen production.

Author Contributions: Conceptualization, M.A.; methodology, M.A.; software, T.U. and M.A.; validation, T.U. and M.A.; formal analysis, T.U., M.A. and T.M.; investigation, T.U., M.A. and T.M.; resources, M.A. and T.M.; data curation, T.U., M.A. and T.M.; writing—original draft preparation, T.U., M.A. and T.M.; writing, T.U., M.A. and T.M.; visualization, T.U. and M.A.; supervision, M.A.; funding acquisition, M.A. All authors have read and agreed to the published version of the manuscript.

Funding: This research was funded in part by the Paloma Environmental Technology Development Foundation.

Data Availability Statement: The data presented in this study are available on request from the corresponding author. The data are not publicly available due to privacy protection and ethical considerations.

Conflicts of Interest: The authors declare no conflict of interest.

References

1. Kabeyi, M.J.B.; Olanrewaju, O.A. Sustainable energy transition for renewable and low carbon grid electricity generation and supply. *Front. Energy Res.* **2022**, *9*, 743114. [CrossRef]
2. Abbasi, K.R.; Shahbaz, M.; Zhang, J.; Irfan, M.; Alvarado, R. Analyze the environmental sustainability factors of China: The role of fossil fuel energy and renewable energy. *Renew. Energy* **2022**, *187*, 390–402. [CrossRef]
3. Xiong, J.; Xu, D. Relationship between energy consumption, economic growth and environmental pollution in China. *Environ. Res.* **2021**, *194*, 110718. [CrossRef]
4. Xia, W.; Apergis, N.; Bashir, M.F.; Ghosh, S.; Doğan, B.; Shahzad, U. Investigating the role of globalization, and energy consumption for environmental externalities: Empirical evidence from developed and developing economies. *Renew. Energy* **2022**, *183*, 219–228. [CrossRef]
5. Yusaf, T.; Laimon, M.; Alrefae, W.; Kadirgama, K.; Dhahad, H.A.; Ramasamy, D.; Kamarulzaman, M.K.; Yousif, B. Hydrogen energy demand growth prediction and assessment (2021–2050) using a system thinking and system dynamics approach. *Appl. Sci.* **2022**, *12*, 781. [CrossRef]
6. Wijayasekera, S.C.; Hewage, K.; Siddiqui, O.; Hettiaratchi, P.; Sadiq, R. Waste-to-hydrogen technologies: A critical review of techno-economic and socio-environmental sustainability. *Int. J. Hydrogen Energy* **2022**, *47*, 5842–5870. [CrossRef]
7. Janoszek, T.; Masny, W. CFD simulations of allothermal steam gasification process for hydrogen production. *Energies* **2021**, *14*, 1532. [CrossRef]
8. Muradov, N.; Smith, F.; Huang, C.; T-Raissi, A. Autothermal catalytic pyrolysis of methane as a new route to hydrogen production with reduced CO_2 emissions. *Catal. Today* **2006**, *116*, 281–288. [CrossRef]
9. Takenaka, S.; Shigeta, Y.; Tanabe, E.; Otsuka, K. Methane decomposition into hydrogen and carbon nanofibers over supported Pd-Ni catalysts. *J. Catal.* **2003**, *220*, 468–477. [CrossRef]

10. Zhou, L.; Basset, J.M. Unsupported Ni–Pt alloy metal catalysts prepared by water-in-oil (W/O) microemulsion method for methane cracking. *Fuel* **2016**, *181*, 805–810. [CrossRef]
11. Mei, I.L.S.; Lock, S.S.M.; Vo, D.V.N.; Abdullah, B. Thermo-catalytic methane decomposition for hydrogen production: Effect of palladium promoter on Ni-based catalysts. *Bull. Chem. React. Eng. Catal.* **2016**, *11*, 191–199. [CrossRef]
12. Ouyang, M.; Boldrin, P.; Maher, R.C.; Chen, X.; Liu, X.; Cohen, L.F.; Brandon, N.P. A mechanistic study of the interactions between methane and nickel supported on doped ceria. *Appl. Catal. B Environ.* **2019**, *248*, 332–340. [CrossRef]
13. Chen, J.; Li, Y.; Li, Z.; Zhang, X. Production of CO_x-free hydrogen and nanocarbon by direct decomposition of undiluted methane on Ni–Cu–alumina catalysts. *Appl. Catal. A Gen.* **2004**, *269*, 179–186. [CrossRef]
14. Ermakova, M.A.; Ermakov, D.Y.; Kuvshinov, G.G. Effective catalysts for direct cracking of methane to produce hydrogen and filamentous carbon. Part I. Nickel catalysts. *Appl. Catal. A Gen.* **2000**, *201*, 61–70. [CrossRef]
15. Bayat, N.; Rezaei, M.; Meshkani, F. Methane decomposition over Ni–Fe/Al_2O_3 catalysts for production of CO_x-free hydrogen and carbon nanofiber. *Int. J. Hydrogen Energy* **2016**, *41*, 1574–1584. [CrossRef]
16. Ashik, U.P.M.; Wan Daud, W.M.A.; Abbas, H.F. Production of greenhouse gas free hydrogen by thermocatalytic decomposition of methane—A review. *Renew. Sustain. Energy Rev.* **2015**, *44*, 221–256. [CrossRef]
17. Li, Y.; Li, D.; Wang, G. Methane decomposition to CO_x-free hydrogen and nano-carbon material on group 8–10 base metal catalysts: A review. *Catal. Today* **2011**, *162*, 1–48. [CrossRef]
18. Zhang, C.; Zhang, W.; Drewett, N.E.; Wang, X.; Yoo, S.J.; Wang, H.; Deng, T.; Kim, J.G.; Chen, H.; Huang, K.; et al. Integrating catalysis of methane decomposition and electrocatalytic hydrogen evolution with Ni/CeO_2 for improved hydrogen production efficiency. *ChemSusChem* **2019**, *12*, 1000–1010. [CrossRef]
19. Pudukudy, M.; Yaakob, Z.; Jia, Q.; Takriff, M.S. Catalytic decomposition of methane over rare earth metal (Ce and La) oxides supported iron catalysts. *Appl. Surf. Sci.* **2019**, *467–468*, 236–248. [CrossRef]
20. Urdiana, G.; Valdez, R.; Lastra, G.; Valenzuela, M.Á.; Olivas, A. Production of hydrogen and carbon nanomaterials using transition metal catalysts through methane decomposition. *Mater. Lett.* **2018**, *217*, 9–12. [CrossRef]
21. Gao, W.; Zhu, Q.; Ma, D. Nanostructured catalyst for Fischer–Tropsch synthesis. *Chin. J. Chem.* **2018**, *36*, 798–808. [CrossRef]
22. Awadallah, A.E.; El-Desouki, D.S.; Abdel-Azim, S.M.; Aboul-Gheit, N.A.K.; Abdel-Hamid, S.M.; Aboul-Gheit, A.K. Effect of La, Ce and Nd oxides addition on the activity and stability of Co/MgO catalyst for methane decomposition into CO_x-free H_2 production and carbon nanotubes. *Fuller. Nanotub. Carbon Nanostruct.* **2018**, *26*, 525–534. [CrossRef]
23. Awadallah, A.E.; Aboul-Enein, A.A.; Mahmoud, A.H.; Abd El Rehim, S.S.; El-Ziaty, A.K.; Aboul-Gheit, A.K. $Zr_xMg_{1-x}O$ supported cobalt catalysts for methane decomposition into CO_x-free hydrogen and carbon nanotubes. *Int. J. Green Energy* **2018**, *15*, 568–576. [CrossRef]
24. Zhou, L.; Enakonda, L.R.; Saih, Y.; Loptain, S.; Gary, D.; Del-Gallo, P.; Basset, J.M. Catalytic methane decomposition over Fe–Al_2O_3. *ChemSusChem* **2016**, *9*, 1243–1248. [CrossRef]
25. Qian, J.X.; Chen, T.W.; Enakonda, L.R.; Liu, D.B.; Mignani, G.; Basset, J.M.; Zhou, L. Methane decomposition to produce CO_x-free hydrogen and nano-carbon over metal catalysts: A review. *Int. J. Hydrogen Energy* **2020**, *45*, 7981–8001. [CrossRef]
26. Cunha, A.F.; Órfão, J.J.M.; Figueiredo, J.L. Methane decomposition on Ni–Cu alloyed Raney-type catalysts. *Int. J. Hydrogen Energy* **2009**, *34*, 4763–4772. [CrossRef]
27. Chambers, A.; Nemes, T.; Rodriguez, N.M.; Baker, R.T.K. Catalytic behavior of graphite nanofiber supported nickel particles. 1. Comparison with other support media. *J. Phys. Chem. B* **1998**, *102*, 2251–2258. [CrossRef]
28. Cunha, A.F.; Órfão, J.J.M.; Figueiredo, J.L. Methane decomposition on Fe–Cu Raney-type catalysts. *Fuel Process. Technol.* **2009**, *90*, 1234–1240. [CrossRef]
29. Lua, A.C.; Wang, H.Y. Hydrogen production by catalytic decomposition of methane over Ni–Cu–Co alloy particles. *Appl. Catal. B Environ.* **2014**, *156–157*, 84–93. [CrossRef]
30. Billaud, F.; Gueret, C.; Weill, J. Thermal decomposition of pure methane at 1263 K. Experiments and mechanistic modelling. *Thermochim. Acta* **1992**, *211*, 303–322. [CrossRef]
31. Wang, S.; Wen, Y.; Shi, Z.; Zaini, I.N.; Jonsson, P.G.; Yang, W. Novel carbon-negative methane production via integrating anaerobic digestion and pyrolysis of organic fraction of municipal solid waste. *Energy Convers. Manag.* **2022**, *252*, 115042. [CrossRef]
32. Sun, E.; Zhai, S.; Kim, D.; Gigantino, M.; Haribal, V.; Dewey, O.S.; Williams, S.M.; Wan, G.; Nelson, A.; Marin-Quiros, S.; et al. A semi-continuous process for co-production of CO_2-free hydrogen and carbon nanotubes via methane pyrolysis. *Cell Rep. Phys. Sci.* **2023**, *4*, 101338. [CrossRef]
33. Patel, S.; Kundu, S.; Halder, P.; Marzbali, M.H.; Chiang, K.; Surapaneni, A.; Shah, K. Production of hydrogen by catalytic methane decomposition using biochar and activated char produced from biosolids pyrolysis. *Int. J. Hydrogen Energy* **2020**, *45*, 29978–29992. [CrossRef]
34. Yousefi, M.; Donne, S. Experimental study for thermal methane cracking reaction to generate very pure hydrogen in small or medium scales by using regenerative reactor. *Front. Energy Res.* **2022**, *10*, 971383. [CrossRef]
35. New Energy and Industrial Technology Development Organization (NEDO). *NEDO Hydrogen and Fuel Cell Project Review 2021, Hydrogen Technology in General (Leading R&D)*; NEDO Final Report; New Energy and Industrial Technology Development Organization (NEDO): Kawasaki, Japan, 2021.
36. Muradov, N.; Veziroğlu, T. "Green" path from fossil-based to hydrogen economy: An overview of carbon-neutral technologies. *Int. J. Hydrogen Energy* **2008**, *33*, 6804–6839. [CrossRef]

37. Cheon, S.; Byun, M.; Lim, D.; Lee, H.; Lim, H. Parametric study for thermal and catalytic methane pyrolysis for hydrogen production: Techno-economic and scenario analysis. *Energies* **2021**, *14*, 6102. [CrossRef]
38. Cantera Developers. Reactors and Reactor Networks. Available online: https://cantera.org/science/reactors/reactors.html (accessed on 20 October 2023).
39. Shimizu, K.; Hibi, A.; Koshi, M.; Morii, Y.; Tsuboi, N. Updated kinetic mechanism for high-pressure hydrogen combustion. *J. Propuls. Power* **2011**, *27*, 383–395. [CrossRef]
40. Ranzi, E.; Frassoldati, A.; Grana, R.; Cuoci, A.; Faravelli, T.; Kelley, A.P.; Law, C.K. Hierarchical and comparative kinetic modeling of laminar flame speeds of hydrocarbon and oxygenated fuels. *Prog. Energy Combust. Sci.* **2012**, *38*, 468–501. [CrossRef]
41. Muto, T.; Asahara, M.; Miyasaka, T.; Asato, K.; Uehara, T.; Koshi, M. Methane pyrolysis characteristics for the practical application of hydrogen production system using permalloy plate catalyst. *Chem. Eng. Sci.* **2023**, *274*, 117931. [CrossRef]
42. Abbas, H.F.; Wan Daud, W.M.A. Hydrogen production by methane decomposition: A review. *Int. J. Hydrogen Energy* **2010**, *35*, 1160–1190. [CrossRef]
43. Shirsath, A.B.; Mokashi, M.; Lott, P.; Muller, H.; Pashminehazar, R.; Sheppard, T.; Tischer, S.; Maier, L.; Grunwaldt, J.D.; Deutschmann, O. Soot formation in methane pyrolysis reactor: Modeling soot growth and particle characterization. *J. Phys. Chem. A* **2023**, *127*, 2136–2147. [CrossRef]
44. Abanades, A.; Ruiz, E.; Ferruelo, E.M.; Hernández, F.; Cabanillas, A.; Martínez, J.M.; Rubio, J.A.; López, C.; Gavela, R.; Barrera, G.; et al. Experimental analysis of direct thermal methane cracking. *Int. J. Hydrogen Energy* **2011**, *36*, 12877–12886. [CrossRef]
45. Muradov, N.Z.; Veziroğlu, T.N. From hydrocarbon to hydrogen–carbon to hydrogen economy. *Int. J. Hydrogen Energy* **2005**, *30*, 225–237. [CrossRef]
46. Holmen, A.; Olsvik, O.; Rokstad, O.A. Pyrolysis of natural gas: Chemistry and process concepts. *Fuel Process. Technol.* **1995**, *42*, 249–267. [CrossRef]
47. Arutyunov, V.S.; Vedeneev, V.I. Pyrolysis of methane in the temperature range 1000–1700 K. *Russ. Chem. Rev.* **1991**, *60*, 1384. [CrossRef]
48. Choudhary, T.V.; Aksoyiu, E.; Goodman, D.W. Nonoxidative activation of methane. *Catal. Rev.* **2003**, *45*, 151–203. [CrossRef]
49. Geißler, T.; Abánades, A.; Heinzel, A.; Mehravaran, K.; Müller, G.; Rathnam, R.K.; Rubbia, C.; Salmieri, D.; Stoppel, L.; Stückrad, S.; et al. Hydrogen production via methane pyrolysis in a liquid metal bubble column reactor with a packed bed. *Chem. Eng. J.* **2016**, *299*, 192–200. [CrossRef]
50. Pérez, B.J.L.; Jiménez, J.A.M.; Bhardwaj, R.; Goetheer, E.; van Sint Annaland, M.; Gallucci, F. Methane pyrolysis in a molten gallium bubble column reactor for sustainable hydrogen production: Proof of concept & techno-economic assessment. *Int. J. Hydrogen Energy* **2021**, *46*, 4917–4935. [CrossRef]
51. Murata, K.; Fujita, K.; Uchida, K. Production of hydrogen by pyrolysis of methane over Ni/Ca/carbon catalysts. *J. Japan Pet. Inst.* **1997**, *40*, 129–133. [CrossRef]
52. Kushch, S.D.; Muradyan, V.E.; Fursikov, P.V.; Knerelman, E.I.; Kuznetsov, V.L.; Butenko, Y.V. Methane pyrolysis over carbon catalysts. *Eurasian Chem. Technol. J.* **2001**, *3*, 67–72. [CrossRef]